IEEE Photonics Journal
An IEEE Photonics Society Publication

Open Access

A Heterogeneous Silicon on Lithium Niobate Modulator for Ultra-Compact and High-Performance Photonic Integrated Circuits

Volume 13, Number 1, February 2021

Jing Wang
Shaofu Xu
Jianping Chen
Weiwen Zou, ***Member, IEEE***

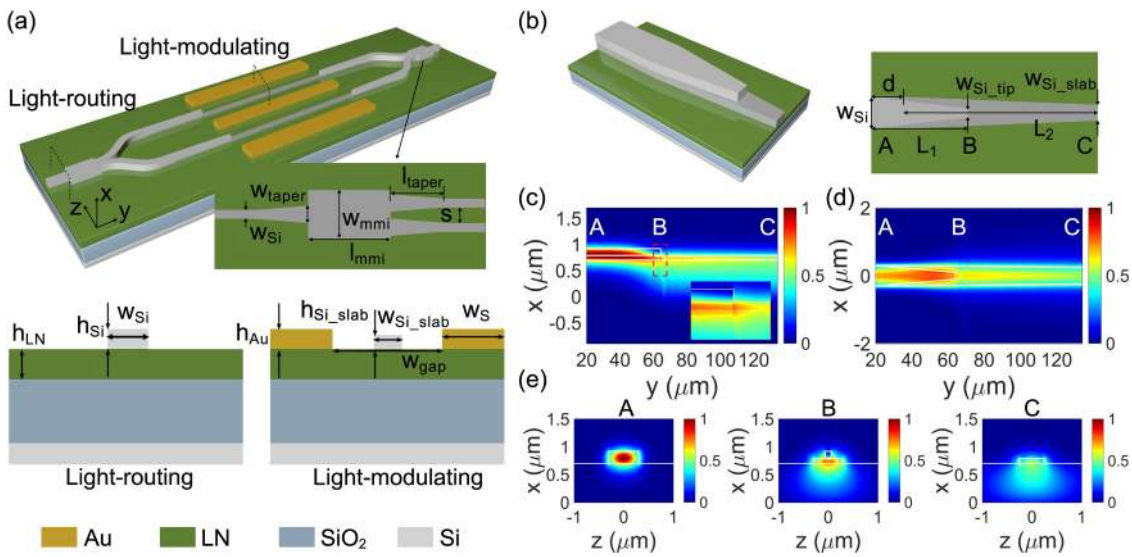

DOI: 10.1109/JPHOT.2020.3048690

A Heterogeneous Silicon on Lithium Niobate Modulator for Ultra-Compact and High-Performance Photonic Integrated Circuits

Jing Wang, Shaofu Xu, Jianping Chen, and Weiwen Zou, *Member, IEEE*

State Key Laboratory of Advanced Optical Communication Systems and Networks, Intelligent Microwave Lightwave Integration Innovation Center (iMLic), Department of Electronic Engineering, Shanghai Jiao Tong University, 800 Dongchuan Road, Shanghai 200240, China

DOI:10.1109/JPHOT.2020.3048690

Manuscript received November 24, 2020; revised December 17, 2020; accepted December 29, 2020. Date of publication January 1, 2021; date of current version January 21, 2021. This work was supported in part by the National Key R&D Program of China under Program 2019YFB2203700 and in part by the National Natural Science Foundation of China under Grant 61822508. Corresponding author: Weiwen Zou (e-mail: wzou@sjtu.edu.cn).

Abstract: We propose a heterogeneous silicon on lithium niobate (Si-LN) modulator which improves the compactness and modulating performance of large-scale photonic integrated circuits. Two types of configurations are employed on the Si-LN wafer for ultra-compact light-routing waveguides and high-performance light-modulating waveguides, respectively. The low loss taper transfers the optical modes between the two waveguides. In the heterogeneous Si-LN modulator, LN etching is nonessential and thus device processes are supported on a robust wafer. Our design analyzes the influence of the LN thickness on the performance. According to theoretical analysis and numerical simulation, the modulator supports a bend radius of 10 μm and edge-to-edge waveguide separation of 0.7 μm with respect to $\sim$1 cm beat length. When thickness of LN is 700 nm, the modulation efficiency reaches 1.76 V$\cdot$cm and the bandwidth exceeds 350 GHz. This modulator is potentially suitable for ultra-compact, large-scale, high efficiency, and large bandwidth photonic integrated circuits (PICs).

Index Terms: Heterogenous integration, waveguide devices, electro-optic modulator.

1. Introduction

Integration technology has inspired the advanced applications in large-scale PICs such as microwave photonics [1]–[3] and optical neural network [4]–[6], where numerous electro-optic modulators and routing waveguides are integrated. Ideally, such applications require electro-optic modulators with high modulation efficiency and a large bandwidth. Additionally, compact PICs can be expected with waveguides supporting a small bend radius and tight edge-to-edge separation with negligible crosstalk. Although PICs with modulators can be fabricated with a silicon-on-isolator (SOI) wafer on which the electro-optic modulator is formed by p-n junction. In terms of Si-based modulators, the performance is limited by a low modulation bandwidth, nonlinearity, and a high loss [7]. Up to date, lithium niobate (LN) is the most promising material for modulators in that LN enables

strong Pockels effect. However, modulators based on bulk LN have a low confinement for the optical mode, resulting in large footprints and low modulation efficiency [8], [9]. These shortcomings make bulk LN-based modulators incompatible with complex PICs.

Recently, as the development of fabrication technology, modulators based on the thin-film LN platform have been realized, demonstrating the potential of complex PICs. A phase shifter is an important structure for a modulator. Several types of phase shifter structures have been introduced, such as LN ridge [10]–[12] and hybrid waveguides. The latter uses LN on SOI (LN-SOI) configuration [13]–[15] or SOI on LN (SOI-LN) configuration [16]–[19]. The strip-loaded waveguide with LN-SOI configuration is designed for modulator to avoid LN etching. This device achieves a modulation bandwidth of 106 GHz and modulation efficiency of 6.7 V·cm [14]. Such an approach involves deposition, waveguide patterning, and pieces of LN bonding. Modulators with SOI-LN configuration require no LN etching. This approach typically involves fabrication of silicon (Si) or silicon nitride (SiN_x) waveguides on the top of a thin-film LN wafer, enabling robust device processes based on a full wafer instead of pieces of LN bonding [19]. Works of this approach have been demonstrated with modulation efficiency of 2.1 V·cm. However, the bend radius of the SiN_x-LN waveguide can reach 300 μm, leading to a large footprint which limits the integration density.

In order to achieve ultra-compact and high-performance modulators for complex PICs, we propose a novel electro-optic modulator which jointly utilizes the high refractive index of Si and the superior electro-optic property of LN. The proposed modulator consists of light-routing waveguides and light-modulating waveguides on the Si-LN wafer. Light is mainly confined to the Si layer or the LN layer so as to be routed or modulated. Thus, dimensions of Si and the electrode are optimized to achieve ultra-compact routing and high-performance modulating for transverse-electric (TE) polarized single-mode. Additionally, the thickness of LN is studied, and analysis procedures for such device are presented. We evaluate the performance of the proposed modulator against the bend radius, the edge-to-edge waveguide separation, the modulating efficiency, and the bandwidth. Consequently, the modulation efficiency reaches 1.76 V·cm and the modulation bandwidth exceeds 350 GHz. And the bend radius is 30 times lower than the mostly recent result [19]. Our work can pave the way to ultra-compact, high-efficiency and large bandwidth PICs on the heterogenous Si-LN platform for future microwave photonics and optical neural network, where large-scale electro-optic modulators are essential components.

2. Design of the Light-Routing Waveguide and the Light-Modulating Waveguide

The structure schematic of the Si-LN Mach-Zehnder electro-optic modulator is shown in Fig. 1(a). This modulator is designed on the monocrystalline Si-LN wafer which can be fabricated by wafer bonding. This modulator consists of two light-modulating waveguides as phase shifters, two multimode interferences (MMIs) as couplers, and light-routing waveguides. Since there are multiple bend waveguides and parallel waveguides in complex PICs using modulators, it is critical to realize ultra-compact light-routing waveguides and high-performance light-modulating waveguides. Compared with Si, LN has a lower refractive index and strong Pockels effect. As a result, normal Si strips support tight structures, while it prevents optical confinement in thin-film LN and leads to weak Pockels effect. Therefore, it is necessary to make different Si dimensions for different parts of this Mach-Zehnder electro-optic modulator, as shown in the cross section of Fig. 1(a). In this way, different parts of this modulator can support different modes. Another important part of this modulator is the mode transition taper between the light-routing waveguide and the light-modulating waveguide. Through the mode transition taper, optical mode accesses into thin-film LN to perform electro-optic modulating. At the tail of the modulating waveguide, most of the optical mode is transferred back into Si for tight bend and parallel waveguides.

In this work, we optimize the Si dimensions on the x-cut LN wafer obtained from NanoLN. The thickness of LN is set as 700 nm. Based on the requirement of ultra-compact and high-performance

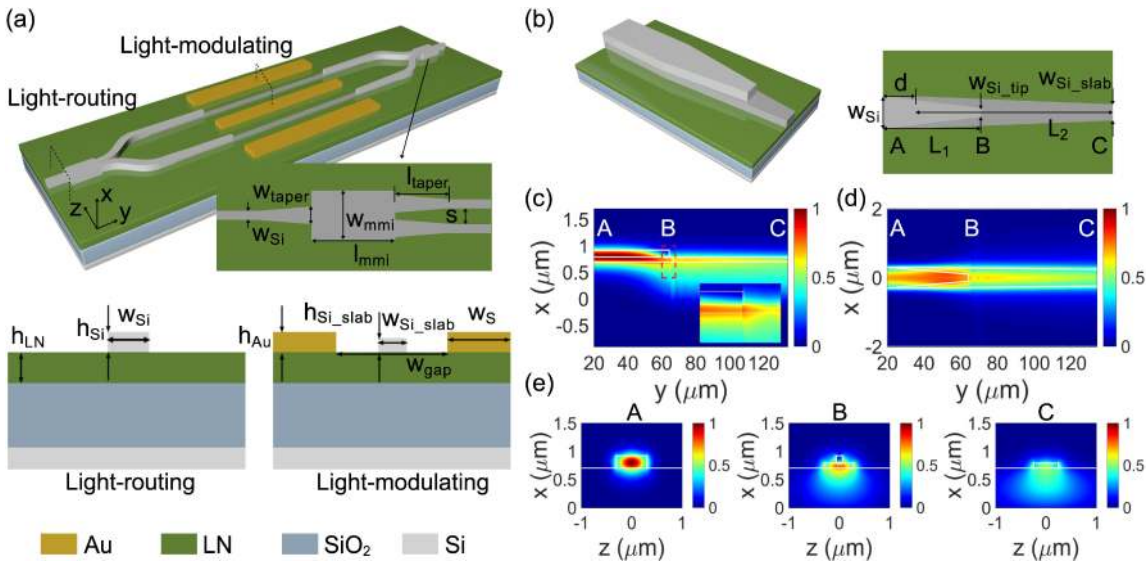

Fig. 1. (a) The 3D structure of Si-LN Mach-Zehnder electro-optic modulator as well as the cross section of the light-routing waveguide and the light-modulating waveguide. (b) The 3D structure and the top view of bilevel taper connecting the light-routing waveguide and the light-modulating waveguide. (c) The cross view of the optical TE mode transition of bilevel taper, the insert in the right donates the mode transition located at the tip of the upper taper. (d) The top view of the optical TE mode transition of bilevel taper. (e) Calculated optical TE mode distributions associated at different positions (A, B, C). Position A is located at the input-port of taper. Position B is located at the tip of upper taper. Position C is located at the tip of lower taper.

PICs, we design the modulator in terms of four major factors of the effective refractive index, the mode area, the optical mode confinement in thin-film LN (Γ_{LN}) and the metal-induced loss. The first three factors are determined by Si dimensions including width and height. The metal-induced loss is also affected by the metal electrodes beside the light-modulating waveguides. The high effective refractive index and the small mode area enables a small bend radius and tight waveguide separation for ultra-compact light-routing waveguides. The large optical mode confinement in thin-film LN and metal-induced loss are desirable for high efficiency and low loss light-modulating waveguides. We optimize the dimensions of Si with four major factors with the assistance of commercial Lumerical solutions. As shown in Fig. 2, the effective refractive index (Fig. 2(a)), the mode area (Fig. 2(b)), the Γ_{LN} (Fig. 2(c)), and the metal-induced loss (Fig. 2(d)) are simulated to show their respective variation with the dimensions of Si. Considering the single mode condition, Si of 600 nm wide and 220 nm tall features the small mode area and the high effective refractive index. In order to achieve balance between the large Γ_{LN} and the target metal-induced loss, Si of 480 nm wide and 90 nm tall is selected (A gap of 4.5 μm is set between the signal electrode and the ground electrode. The target metal-induced loss is $\sim$0.6 dB/cm.). The losses of this modulator are mainly attributed to the metal-induced loss and the scattering losses, which depend on the size of the waveguide and the roughness of the sidewall [20].

Since the routing and modulating waveguides in this structure are of different widths and heights, a bilevel taper designed by etching Si is adopted [21], [22], as shown in Fig. 1(b). The lower layer is a transition with a height of $h_{\mathrm{Si\_slab}} = 90$ nm and a width from $w_{\mathrm{Si}} = 600$ nm to $w_{\mathrm{Si\_slab}} = 480$ nm over a length of $L_1 = 44.2$ μm. The upper layer is a taper with a height of 130 nm, width from $w_{\mathrm{Si}} = 600$ nm to $w_{\mathrm{Si\_tip}} = 120$ nm over a length of $L_2 = 102.2$ μm. Along the propagation, there is $d = 12$ μm between the lower and upper transitions. Simulation is performed in FDTD solutions to analyze the bilevel taper. Propagation and distribution of the optical TE mode are illustrated in Fig. 1(c) and Fig. 1(d), respectively. The simulated coupling efficiency of the bilevel taper is

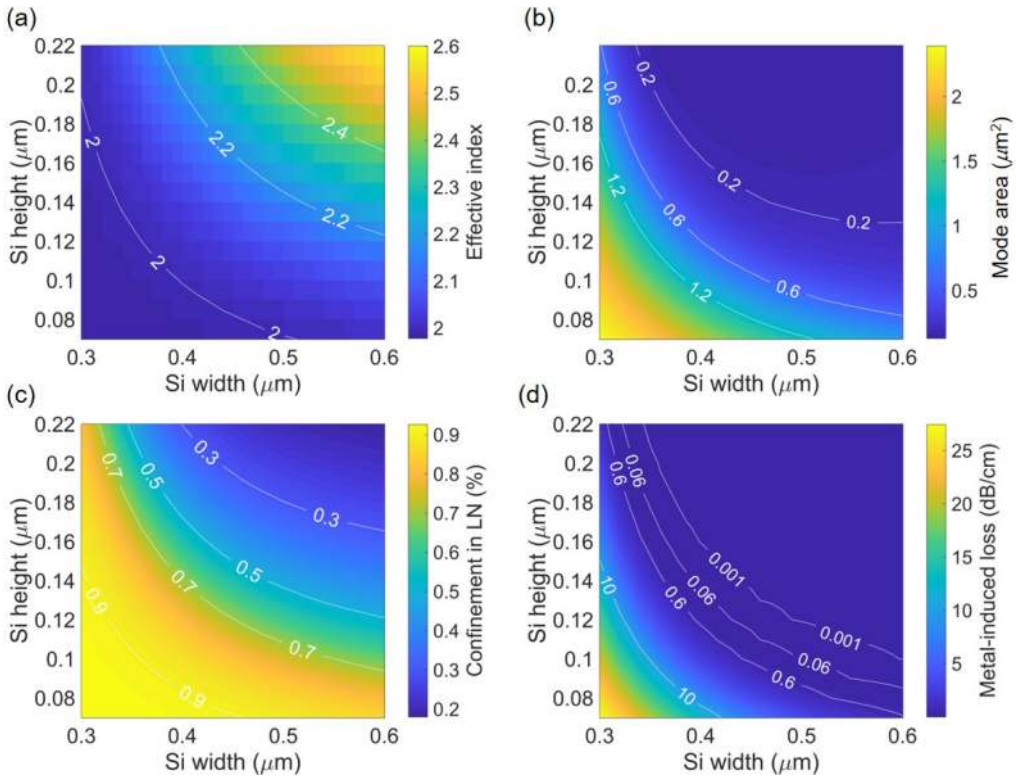

Fig. 2. Si dimensions affect the characteristic of the Si-LN waveguide with (a) the effective refractive index, (b) the mode area, (c) the optical confinement in thin-film LN, and (d) the metal-induced loss.

$\sim$98.6%. The loss of the bilevel taper is mainly attributed to the mode mismatch located at the tip of the upper taper. It should be noted that the taper can be placed between the light-routing waveguide and the optical-modulating waveguide for mode transition. This is compatible with the present fabrication processes.

MMIs are adopted to split the input light into both arms of the modulator and then couple it at the output. Here we set the MMI section with a width of $w_{\mathrm{mmi}} = 2.7$ μm, a length of $l_{\mathrm{mmi}} = 6.6$ μm, and the edge-to-edge separation of $s = 0.7$ μm to avoid evanescent coupling between the two output modes. The length and width of input and output tapers are $l_{\mathrm{taper}} = 10$ μm and $w_{\mathrm{taper}} = 1$ μm, respectively. The simulated insertion loss of the MMI is $\sim$0.06 dB in FDTD solutions. Recent research reported that Si grating couplers could be used for coupling light between fibers and waveguides on the thin-film LN [23]. For further fabrication, Si-LN grating couplers with 220 nm Si are optimized and used.

A coplanar waveguide (CPW) is another critical part to realize travelling wave electrodes with a large modulation bandwidth. Fig. 1(a) shows the cross section of the Si-LN waveguide and the CPW beside the light-modulating waveguide. The CPW structure consists of a signal electrode and two ground electrodes configuring in a ground-signal-ground (GSG) form. The signal electrode is located between two phase shifters of Mach-Zehnder inference. Ground electrodes are located beside two phase shifters. The gap between the signal electrode and the ground electrode strongly affects the modulation efficiency. For this work, $w_{\mathrm{gap}} = 4.5$ μm is chosen. The microwave properties varying with the electrode dimensions are the microwave loss, the microwave impedance, the microwave effective index, and the index mismatch between the microwave effective index and the optical group index. Fig. 3 shows microwave properties (performed at 100 GHz) with the assistance of ANSYS HFSS. When reducing the electrode width and height, it can be indicated

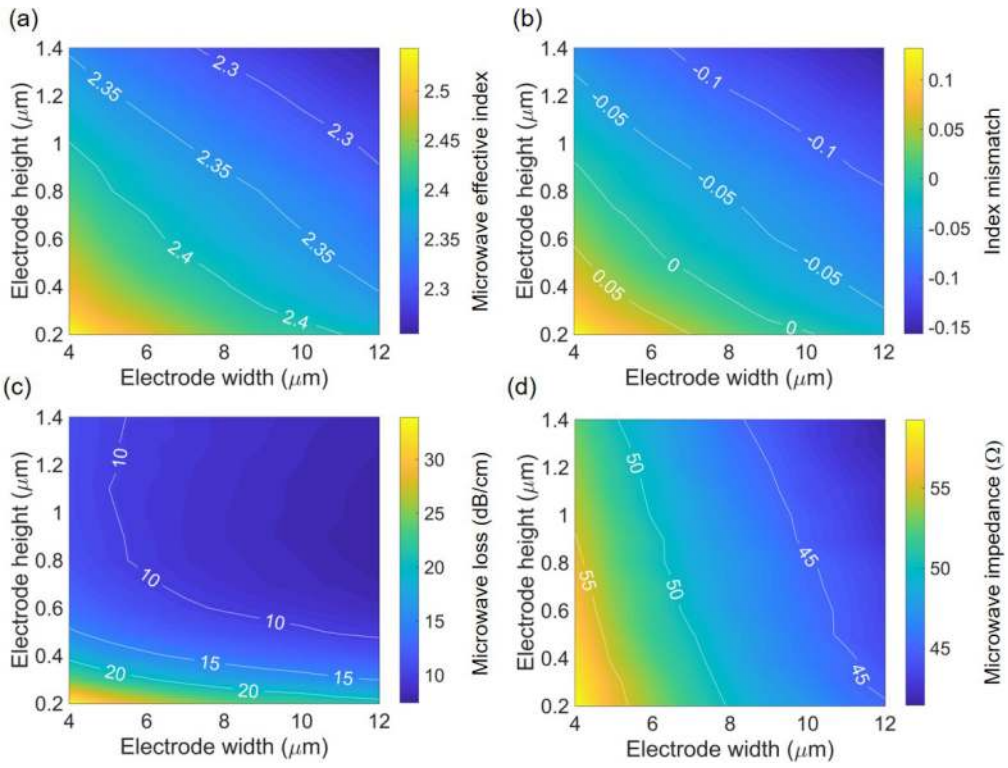

Fig. 3. Electrode dimensions affect the microwave properties with (a) the microwave effective index n_m, (b) the index mismatch between the microwave effective index and the optical group index, (c) microwave loss α_m, and (d) microwave impedance Z_0.

that the microwave effective index and the index mismatch decrease while the microwave loss and impedance increase. For the purpose of a large modulation bandwidth, the height and width of electrodes are optimized for velocity matching and impedance matching. Hence, the thickness of electrodes is set as $h_{Au} = 400$ nm and the width of signal electrode is set as $w_S = 7$ μm.

3. Performance Evaluation

The light-routing waveguide consists of 600 nm wide and 220 nm tall Si on LN. The light-modulating waveguide consists of 480 nm wide and 90 nm tall Si on LN. In the light-routing waveguide, the mode is mostly confined to the Si layer with $\Gamma_{Si} = 76\%$, an effective refractive index of $n_{eff} = 2.6$, and a mode area of 0.16 μm^2 (simulated at 1550 nm). In the light-modulating waveguide, the mode is mostly confined to the thin-film LN layer with $\Gamma_{LN} = 83\%$, an effective refractive index of $n_{eff} = 2.02$, and a mode area of 0.76 μm^2. The bend loss (including mode mismatch and radiation) and beat length of Si-LN waveguides are simulated. Here, our work is compared with the representative structures of ridge LN [12], LN-Si [13], and SiN_x-LN [19], respectively. According to the results shown in Fig. 4(a), the light-routing waveguide can support a small bend radius of 10 μm, much less than those of LN-ridge waveguides, SiN_x-LN waveguides, and light-modulating waveguides. The bend radius of the light-routing waveguide is 10 μm with loss around 0.01 dB/90° bend, which is comparable than that of a standard Si waveguide (600 nm $\times$ 220 nm surrounded by SiO2). We investigate the parallel light-routing waveguides with separation. When the edge-to-edge waveguide separation gradually approaches the limitation of 0 μm, the modes inside adjacent waveguides cause strong coupling, which can be qualified by the beat length $L_C = \lambda_0/2|n_{odd} - n_{even}|$, where n_{odd} is the effective refractive index of the anti-asymmetric mode and n_{even} is the

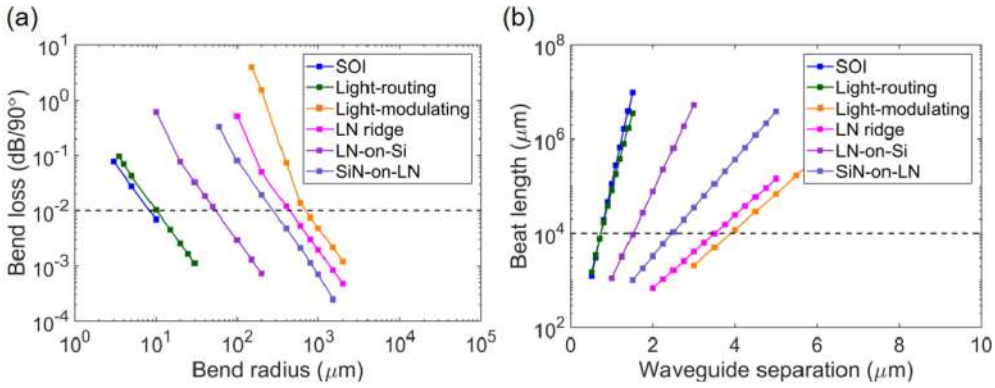

Fig. 4. Performance comparison of Si-LN waveguides for four different structures including our work with LN ridge [12], LN-Si [13], and SiN_x-LN [19]. (a) The waveguide bend loss as the function of the bend radius. (b) The beat length L_c of two parallel waveguides as the function of the (edge-to-edge) waveguide separation.

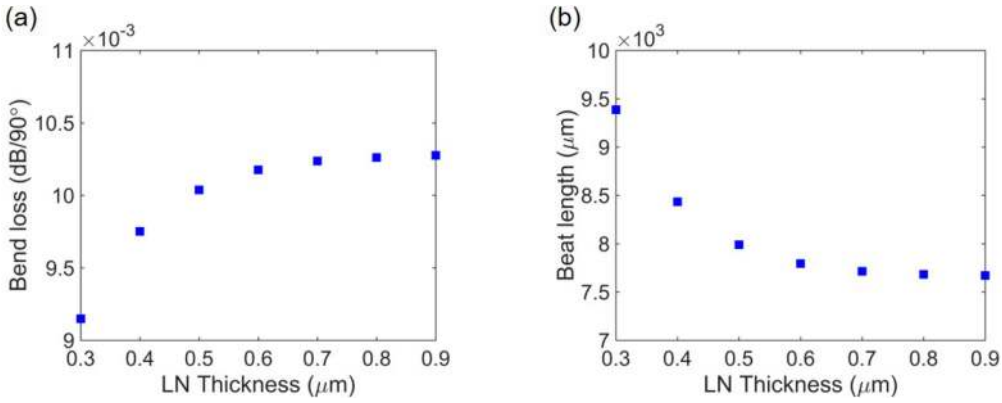

Fig. 5. The simulated (a) bend loss with bend radius of 10 μm and (b) the beat length with waveguide separation of 0.7 μm versus the thickness of LN. The dimensions of the Si waveguide are 600 nm $\times$ 220 nm.

effective refractive index of the asymmetric mode. L_C describes the length for full power transfer from one waveguide to another waveguide. A large L_C implies weak coupling and is associated with lower crosstalk between the two waveguides. As shown in Fig. 4(b), the Si-LN waveguide can support waveguide separation of 0.7 μm with respect to $\sim$1 cm beat length, which is less than those of LN-ridge waveguides, SiNx-LN waveguides, and light-modulating waveguides.

The bend radius and waveguide separation are important figures of merit to qualified compactness of PICs using numerous modulators. The smaller bend radius and the tighter waveguide separation indicate more compact PICs. Here we compare our work based on the Si-LN waveguides with three other structures, including modulators based on the LN-ridge, LN-Si and SiN_x-LN waveguides. According to Fig. 4, a more compact structure is achieved based on the Si-LN waveguides or LN-Si waveguides in that most optical mode is strictly confined in Si. The LN-Si modulator acquires wafer bonding which complicate the device processes, while the robust device processes are supported on the Si-LN wafer. Discussion about the thickness of LN is performed in Fig. 5. Fig. 5(a) shows the bend loss versus the thickness of LN. Fig. 5(b) shows the beat length versus thickness of LN. The separation of Si waveguides is 0.7 μm. There is no significant variation of the bend loss with the thickness of LN since most of the optical mode is confined in the Si waveguide. However, the beat length decreases as the thickness of LN increases.

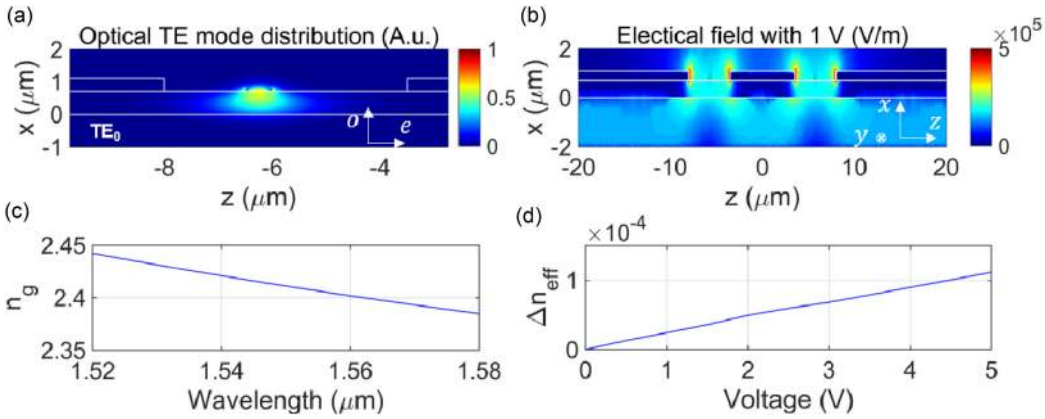

Fig. 6. (a) Cross section of optical TE mode distribution in the optical-modulating waveguide. (b) DC electrical field profile for $V_{DC} = 1$ V around the optical-modulating waveguide. (c) The optical group index. (d) The perturbation of the effective refractive index in the optical-modulating waveguide under applied voltage. The dimensions of the Si waveguide are 480 nm × 90 nm.

Strong electro-optic interaction remains in the light-modulating waveguide with the large optical confinement in the LN layer. Fig. 6(a) shows the optical TE mode distributions in the optical-modulating waveguide. The DC electrical field around the optical-modulating waveguide is shown in Fig. 6(b) when 1 V signal is applied between electrodes. According to the Pockels effect of crystal LN, the inverse permittivity tensor of thin-film LN due to the applied voltage is described as

$$\left[\frac{1}{\varepsilon'_{ij}(x,z)}\right] = \left[\frac{1}{\varepsilon_{ij}}\right] + \left[\Delta\frac{1}{\varepsilon_{ij}}\right] = \begin{bmatrix} \frac{1}{n_{11}^2} & 0 & 0 \\ 0 & \frac{1}{n_{22}^2} & 0 \\ 0 & 0 & \frac{1}{n_{33}^2} \end{bmatrix} + \begin{bmatrix} -r_{22}E_y + r_{13}E_z & -r_{22}E_x & r_{51}E_x \\ -r_{22}E_x & r_{22}E_y + r_{13}E_z & r_{51}E_y \\ r_{51}E_x & r_{51}E_y & r_{33}E_z \end{bmatrix}. \quad (1)$$

where r_{ij} are electro-optic coefficients of LN with reported values of $r_{13} = 8.6$ pm/V, $r_{22} = 3.4$ pm/V, $r_{33} = 30.8$ pm/V, $r_{51} = 28$ pm/V [24]. The E_x and E_z are the in-plane components of the electrical field, whereas the E_y is equal to 0 V/m. The largest electro-optic coefficient r_{33} makes the permittivity tensor perturbation sensitive to applied electrical field, when electrical field is aligned to the extraordinary axis of thin-film LN. Therefore, $n_{11} = n_{22} = n_o = 2.21$ and $n_{33} = n_e = 2.13$, where n_o is the refractive index in LN along the ordinary axis and n_e is the refractive index in LN along the extraordinary axis [24], [25].

The perturbated effective refractive index under the applied electrical field is

$$n'_{ij}(x,z) = \sqrt{\varepsilon'_{ij}(x,z)}. \quad (2)$$

Distribution of the refractive index of the LN is calculated and an optical mode solver (Lumerical Mode Solutions) is employed to find the optical TE mode. The effective refractive index change (Δn_{eff}) of the optical TE mode is defined as the difference between effective refractive index with and without the applied voltage. We calculate the phase shift with push-pull configuration

$$\Delta\phi = \frac{2\pi}{\lambda}\Delta n_{eff} L = \frac{\Delta V}{V_\pi}\frac{\pi}{2}. \quad (3)$$

where λ is the operating wavelength, L is the interaction length in the light-modulating waveguide, V is the applied voltage, and V_π is half-wave voltage. Therefore, we can model the modulating efficiency as $V_\pi L = \Delta V \lambda/(4\Delta n_{eff})$. The Δn_{eff} varies with applied voltage which is depicted in Fig. 6(d). It is clearly linear, yielding halfwave-voltage length product $V_\pi L = 1.76$ V·cm.

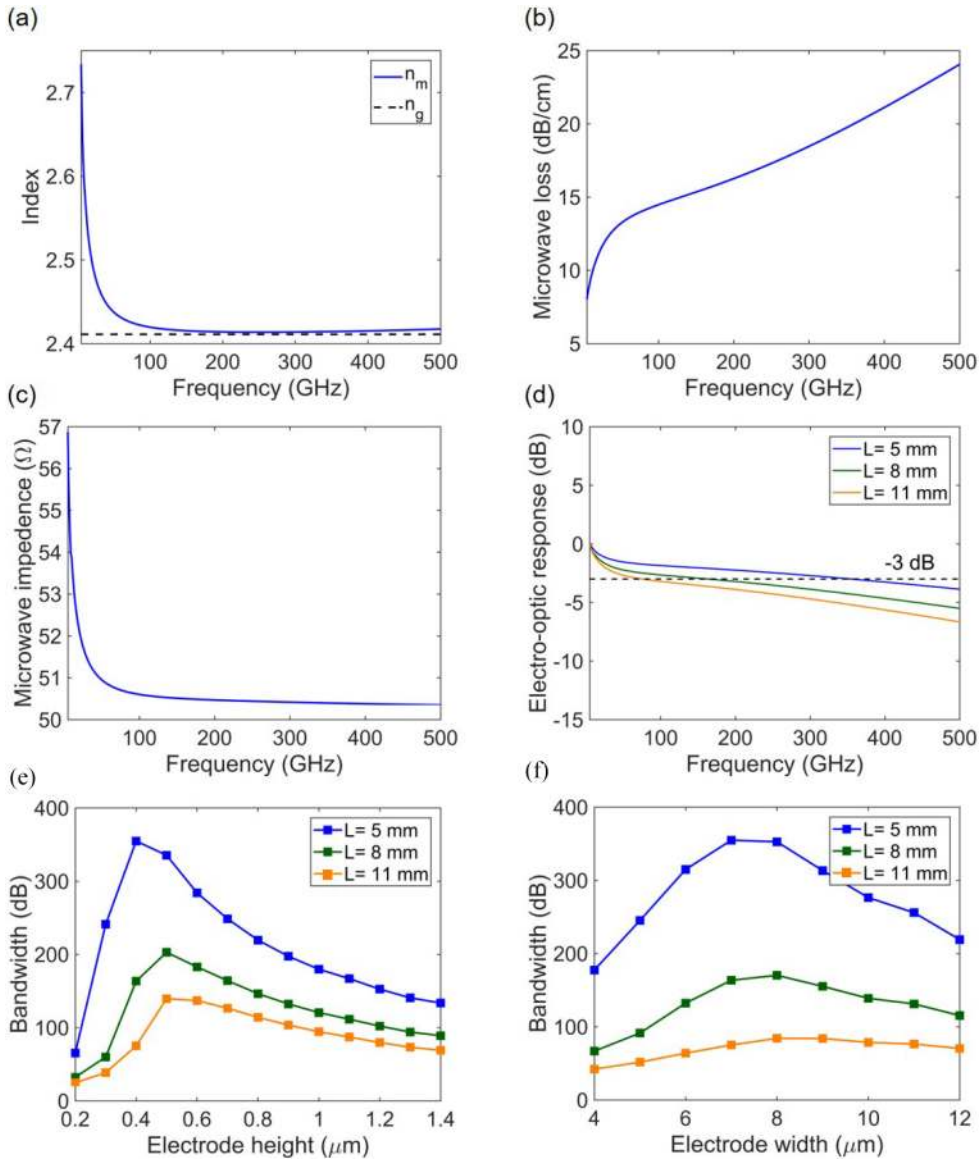

Fig. 7. The simulated (a) microwave effective index n_m and the optical group index n_g, (b) the microwave impedance Z_0, and (c) the microwave loss α_m. (d) Electro-optic response for different interaction lengths. The dark dot line refers to the 3-dB modulation bandwidth. (e) The 3-dB modulation bandwidth versus the height of the electrodes with a width of $w_S = 7$ μm, and (f) The 3-dB modulation bandwidth versus the width of the electrodes with a height of $h_{Au} = 400$ nm.

The electro-optic frequency response $m(\omega)$ at microwave frequency and input impedance Z_{in} can be modeled as [26]

$$m(\omega) = \frac{(Z_L + Z_G)}{Z_L} \left| \frac{Z_{in}}{Z_{in}+Z_G} \right| \left| \frac{(Z_L + Z_0)F(u_+)+(Z_L - Z_0)F(u_-)}{(Z_L + Z_0)e^{(\gamma_m L)} + (Z_L - Z_0)e^{(-\gamma_m L)})} \right|. \quad (4)$$

$$Z_{in} = Z_0 \frac{(Z_L + Z_0 tanh\gamma_m L)}{(Z_0 + Z_L tanh\gamma_m L)}. \quad (5)$$

where Z_L is load impedance, Z_G is generator impedance, and Z_0 is the characterized impedance. $F(u_\pm) = (1 - \exp(u_\pm))/u_\pm$ where $u_\pm = \pm\alpha_m L + j\omega(\pm n_m - n_g)L/c$. The microwave loss α_m and the

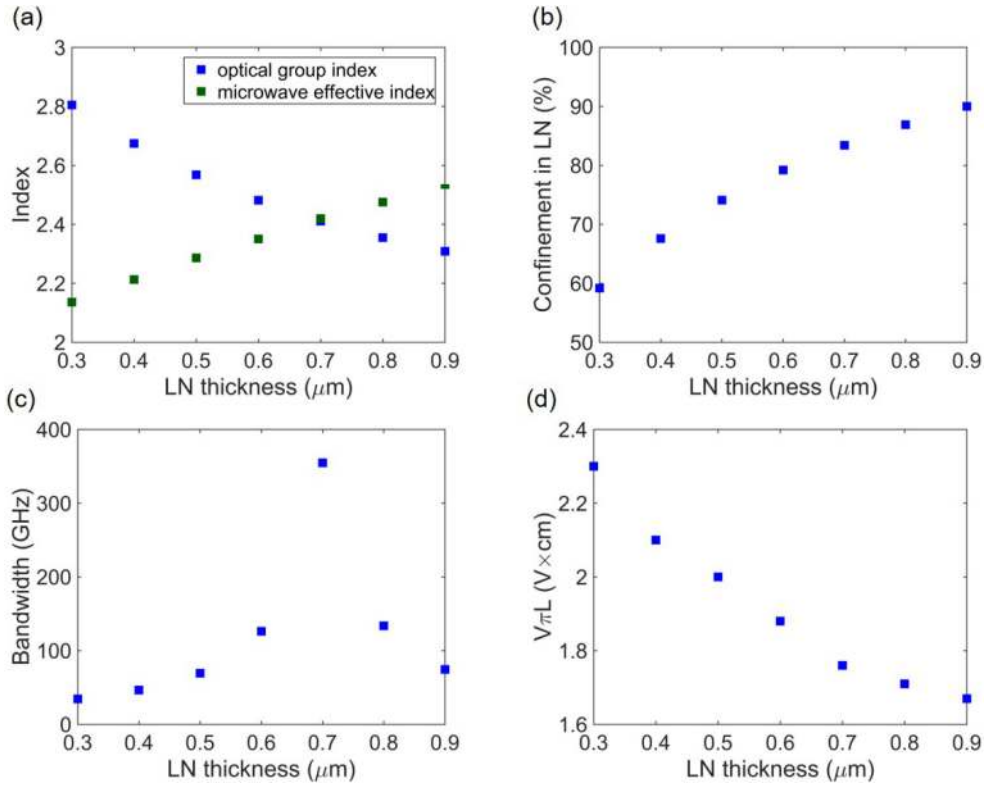

Fig. 8. The simulated (a) index including the optical group index and the microwave effective index at 100 GHz, (b) the optical confinement in thin-film LN, (c) the bandwidth with the electro-optic interaction length of 5 mm, and (d) $V_\pi L$ versus the thickness of LN.

microwave effective mode index n_m attribute to propagation constant $\gamma_m = \alpha_m + j\omega n_m /c$. Here the unit of α_m is Np/cm, and 1 Np/cm is approximately 8.68 dB/cm. We assume that the load and generator impedances equal 50 Ω. According to Eq. (4), the modulation bandwidth is determined by the microwave properties of Z_0, α_m, and n_m and the optical group index of n_g.

Based on the design consideration in Section 2, we adopt LN with a thickness of 700 nm and a signal electrode with a height of 400 nm and a width of 7 μm for simulation. As depicted in Figs. 7(a), the microwave effective index n_m ranges from 2.4 to 2.75 and the optical group index n_g of the optical TE mode (simulated at 1550 nm) is ∼2.41. As depicted in Figs. 7(b) and 7(c), α_m ranges from 5 dB/cm to 25 dB/cm and Z_0 ranges from 50 Ω to 57 Ω. The electro-optic frequency response described by Eq. (4) is plotted in Fig. 7(d). The result shows that a shorter interaction length leads to a larger modulation bandwidth. However, a high value of V_π is applied with a short interaction length. For short interaction lengths of 5 mm and 8 mm, the modeled bandwidth exceeds 350 GHz and 160 GHz, respectively. An impressively low V_π value of ∼1.6 V with a corresponding bandwidth of ∼75 GHz can be achieved with an interaction length of 11 mm. As the results in Fig. 7(e) and 7(f) imply that different interaction lengths correspond to different electrode dimensions. When the modulator has a long interaction length, a larger bandwidth can be achieved by optimizing the width or height of the signal electrode.

The thickness of LN plays an important role in optimizing the $V_\pi L$ and the bandwidth of the modulator. Fig. 8(a) indicates the variation of index including the optical group index and the microwave effective index at 100 GHz with the thickness of LN. The index mismatch achieves the minimum value with the LN thickness of 700 nm which contributes to a large bandwidth. Fig. 8(c) summarizes the bandwidth versus the thickness of LN with an interaction length of 5 mm. A large

TABLE 1
Comparison of the Modulation Performance Among Types of LN-Based Modulators

Modulator type	$V_\pi L$ (V·cm)	Bandwidth (GHz)	Note	Reference
LN ridge	3.8	500	/	[10]
LN ridge	2.2	100	/	[11]
LN ridge*	2.2	> 70	Etched pure LN	[12]
LN-Si	6.7	> 106	Bonded LN to Si	[14]
LN-SiN_x	6.67	30.6	Bonded LN to SiN_x	[15]
SiN_x-LN	3	8	Deposited SiN_x to LN	[16]
SiN_x-LN	3.1	33	Deposited SiN_x to LN	[17]
Si-LN	3.6	420	Deposited SiN_x to LN (novel)	[18]
Si-LN	1.76	> 350	Si on LN (novel)	This work

*Bonded LN to Si while etched pure LN as phase shifters.

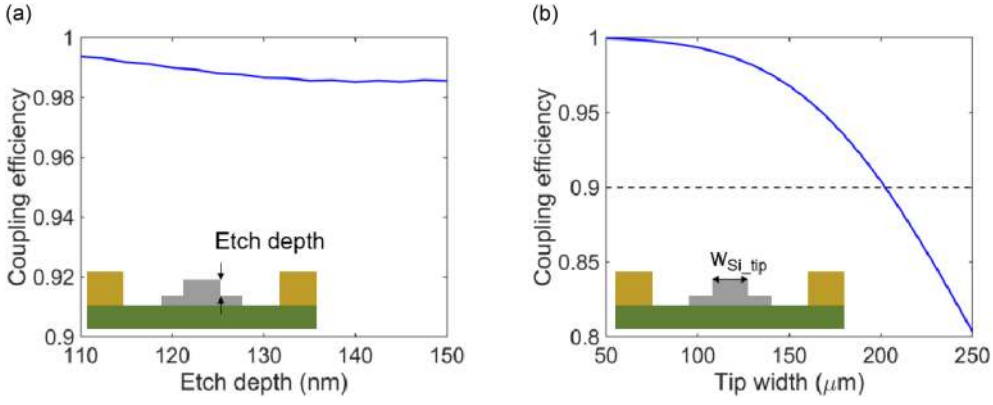

Fig. 9. The simulated coupling efficiency of the bilevel taper against (a) the etch depth and (b) the tip width.

bandwidth exceeding 350 GHz is achieved with the LN thickness of 700 nm. Fig. 8(b) indicates that by increasing the thickness of LN, the optical confinement in LN increases. Lower value of $V_\pi L$ is achieved by increasing the thickness of LN as shown in Fig. 8(d). When the thickness of LN is 900 nm, $V_\pi L$ reaches 1.67 V·cm with a relatively small bandwidth. To the best of our knowledge, such Si-LN modulators on the thin-film LN with the thickness of 700 nm achieve the largest bandwidth of an interaction length of 5 mm. In other words, the ultimate bandwidth is attainable by reducing the interaction length of Si-LN modulators. The value of V_π is lower by reducing the interaction length while maintaining a relatively high Bandwidth.

The influence of the device processes on coupling efficiency of the bilevel taper is simulated. The thickness of the unetched Si layer is as assumed to be 220 nm. According to Fig. 9, the etch depth ranges from70 nm to 110 nm whereas the width of the tip can reach 200 nm with negligible degradation in coupling efficiency. The thickness of the light-modulating waveguide varies with the etch depth, which affects the optical group index of the optical TE mode. The optical group index is an important parameter to predict the modulation bandwidth. The modulation bandwidth is simulated over a range of etch depth and is plotted in Fig. 10. Additional curves are included for the waveguide with a width of 450 nm and 550 nm to illustrate the sensitiveness of the device to this parameter. Additionally, the optical confinement in LN is quite sensitive to the thickness of the light-modulating waveguide. The modulation efficiency is predicted to increase with the etch depth

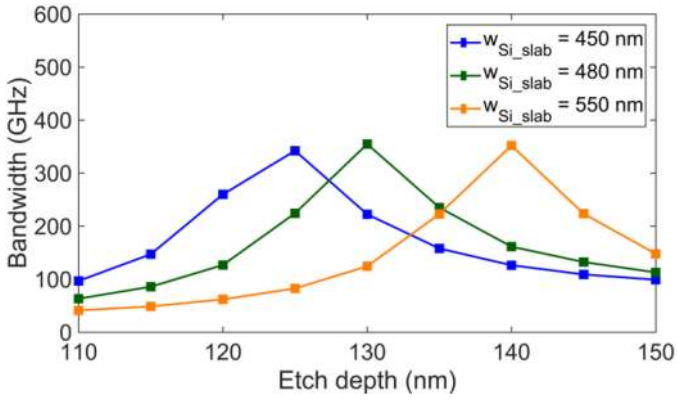

Fig. 10. The simulated bandwidth with the electro-optic interaction length of 5 mm against the etch depth and the width of light modulating waveguide.

because of the growing optical modes confined in the LN layer. However, it is important to take metal-induced loss in case of a large loss of the device.

4. Conclusion

We demonstrate a novel Mach-Zehnder electro-optic modulator configuration consisting of compact routing waveguides of small sizes and high-performance modulating waveguides on the Si-LN wafer without etching and bonding of the thin-film LN. On the thin-film LN with the thickness of 700 nm, the modulation bandwidth exceeds 350 GHz and the modulating efficiency achieves 1.76 V·cm with an interaction length of 5 mm. Meanwhile, the proposed modulators support a bend radius of 10 μm and edge-to-edge waveguide separation of 0.7 μm with respect to $\sim$1 cm beat length. Further device processes include wafer bonding, Si patterning, Si etching, and metal deposition. Another approach without Si patterning is to realize this device on a heterogenous Si-LN wafer. Thus, robust and compatible fabrication technology can be leveraged to enhance the heterogenous integration of ultra-compact and large-scale PICs which demand electro-optic modulators with a large bandwidth and a low value of V_π.

References

[1] C. Lim *et al.*, "Fiber-wireless networks and subsystem technologies," *J. Light. Technol.*, vol. 28, no. 4, pp. 390–405, 2009.
[2] V. R. Supradeepa *et al.*, "Comb-based radiofrequency photonic filters with rapid tunability and high selectivity," *Nat. Photon.*, vol. 6, no. 3, pp. 186–194, 2012.
[3] S. Xu, X. Zou, B. Ma, B. J. Chen, L. Yu, and W. Zou, "Deep-learning-powered photonic analog-to-digital conversion," *Light Sci. Appl.*, vol. 8, no. 66, pp. 1–11, 2019.
[4] Y. Shen *et al.*, "Deep learning with coherent nanophotonic circuits," *Nat. Photon.*, vol. 11, pp. 441–446, 2017.
[5] S. Xu, J. Wang, R. Wang, J. Chen, and W. Zou, "High-accuracy optical convolution unit architecture for convolutional neural networks by cascaded acousto-optical modulator arrays," *Opt. Exp.*, vol. 27, no. 14, pp. 19778–19787, 2019.
[6] S. Xu, J. Wang, and W. Zou, "Optical patching scheme for optical convolutional neural networks based on wavelength-division multiplexing and optical delay lines," *Opt. Lett.*, vol. 45, no. 13, pp. 3689–3692, 2020.
[7] F. Eltes *et al.*, "A batio3-based electro-optic pockels modulator monolithically integrated on an advanced silicon photonics platform," *J. Light. Technol.*, vol. 37, no. 5, pp. 1456–1462, 2019.
[8] R. Tavlykaev, K. Kueckelhaus, and E. Voges, "Index profile reconstruction of ti: Linbo3 structures and bending loss evaluation from near-field measurements," *J. Opt. Telecommun.,* vol. 15, no. 2, pp. 71–76, 1994.
[9] L. Chen, Q. Xu, M. G. Wood, and R. M. Reano, "Hybrid silicon and lithium niobate electro-optical ring modulator," *Optica*, vol. 1, no. 2, pp. 112–118, 2014.
[10] A. J. Mercante, S. Shi, P. Yao, L. Xie, R. M. Weikle, and D. W. Prather, "Thin film lithium niobate electro-optic modulator with terahertz operating bandwidth," *Opt. Exp.*, vol. 26, no. 11, pp. 14810–14816, 2018.
[11] C. Wang *et al.*, "Integrated lithium niobate electro-optic modulators operating at CMOS-compatible voltages," *Nature*, vol. 562, pp. 101–104, 2018.

[12] M. He *et al.*, "High-performance hybrid silicon and lithium niobate mach–zehnder modulators for 100 gbits−1 and beyond," *Nat. Photon.*, vol. 13, no. 5, pp. 359–364, 2019.
[13] E. G. Martin and R. M. Reano, "Design of hybrid silicon and lithium niobate active region for electro-optical modulation," Dept. Elect. Comput. Eng., Electroscience Lab., Ohio State Univ., Columbus, OH, USA. 2017. [Online]. Available: https://apps.dtic.mil/dtic/tr/fulltext/u2/1042219.pdf
[14] P. O. Weigel *et al.*, "Bonded thin film lithium niobate modulator on a silicon photonics platform exceeding 100 GHz 3-dB electrical modulation bandwidth," *Opt. Exp.*, vol. 26, no. 18, pp. 23728–23739, 2018.
[15] N. Boynton *et al.*, "A heterogeneously integrated silicon photonic/lithium niobate travelling wave electro-optic modulator," *Opt. Exp.*, vol. 28, no. 2, pp. 1868–1884, 2020.
[16] S. Jin, L. Xu, H. Zhang, and Y. Li, "LiNbO3 thin-film modulators using silicon nitride surface ridge waveguides," *IEEE Photon. Technol. Lett.*, vol. 28, no. 7, pp. 736–739, Apr. 2016.
[17] A. Rao *et al.*, "High-performance and linear thin-film lithium niobate mach-zehnder modulators on silicon up to 50 GHz," *Opt. Lett.*, vol. 41, no. 24, pp. 5700–5703, 2016.
[18] A. Honardoost, F. Juneghani, R. Safian, and S. Fathpour, "Towards subterahertz bandwidth ultra-compact lithium niobate electrooptic modulators," *Opt. Exp.*, vol. 27, no. 5, pp. 6495–6501, 2019.
[19] A. N. R. Ahmed, S. Nelan, S. Shi, P. Yao, A. J. Mercante, and D. W. Prather, "Subvolt electro-optical modulator on thin-film lithium niobate and silicon nitride hybrid platform," *Opt. Lett.*, vol. 45, no. 5, pp. 1112–1115, 2020.
[20] F. Grillot, L. Vivien, S. Laval, and E. Cassan, "Propagation loss in single-mode ultrasmall square silicon-on-insulator optical waveguides," *J. Lightw. Technol.*, vol. 24, no. 2, pp. 891–896, 2006.
[21] Z. Zou, L. Zhou, X. Li, and J. Chen, "60-nm-thick basic photonic components and Bragg gratings on the silicon-on-insulator platform," *Opt. Exp.*, vol. 23, no. 16, pp. 20784–20795, 2015.
[22] D. Dai, S. He, and H. Tsang, "Bilevel mode converter between a silicon nanowire waveguide and a larger waveguide," *J. Lightw. Technol.*, vol. 24, no. 6, pp. 2428–2433, 2006.
[23] Z. Chen, Y. Wang, H. Zhang, and H. Hu, "Silicon grating coupler on a lithium niobate thin film waveguide," *Opt. Mater. Exp.*, vol. 8, no. 5, pp. 1253–1258, 2018.
[24] A. Yariv and P. Yeh, *Photonics: Optical Electronics in Modern Communications*. Oxford, U.K.: Oxford Univ. Press, 2007.
[25] D. E. Zelmon, D. L. Small, and D. Jundt, "Infrared corrected Sellmeier coefficients for congruently grown lithium niobate and 5 mol.% magnesium oxide-doped lithium niobate," *J. Opt. Soc. Amer. B*, vol. 14, no. 12, pp. 3319–3322, 1997.
[26] G. Ghione, *Semiconductor Devices for High-Speed Optoelectronics*. Oxford, U.K.: Oxford Univ. Press, 2009.